RESEARCH ARTICLE

An Auto-Calibration Algorithm for Hybrid Guided Wave Tomography Based on Full Waveform Inversion

JIAWEI WEN [1,2], **CAN JIANG** [1], **YUBING LI** [1], **HAO CHEN** [1,2], **WEIWEI MA** [1], **AND JIAN WANG** [1], (Member, IEEE)

[1]Institute of Acoustics, Chinese Academy of Sciences, Beijing 100190, China
[2]School of Electronic, Electrical and Communication Engineering, University of Chinese Academy of Sciences, Beijing 100049, China

Corresponding author: Can Jiang (jiangcan@mail.ioa.ac.cn)

ABSTRACT Combining with the dispersion characteristics of ultrasonic guided waves, full waveform inversion method shows great application potential in the quantificational detections of defects in plate- and pipe- like structures. Owing to the inversion efficiency problem, the forward modeling is generally based on the acoustic equation approximation, and a reference signal unaffected by the defects needs to be artificially selected to correct the approximation forward simulation results. This study presents an auto-calibration (without artificial selection of the reference signal) and high-precision imaging method based on the combination of the full waveform inversion and ray tomography algorithm. The ray tomography results are not only used to automatically select the reference signal based on an auto-calibration process, but also used as the macro initial model for the full waveform inversion method, which decreases the possibility of losing in local minimum values during the inversion process and enhances the robustness of the inversion method. Therefore, compared with the classical guided wave tomography method based on full waveform inversion, relatively high-frequency transducers can be used to acquire high-frequency signals, and thus, the imaging accuracy could be effectively improved. Simulation and experiment results have verified that the global relative error of the auto-calibration method is smaller than the classical method. The good imaging results of irregular complex defects confirmed the effectiveness and applicability of the new method.

INDEX TERMS Guided wave, ray tomography, full waveform inversion, auto-calibration.

I. INTRODUCTION

Metal materials play a crucial role in metallurgy, energy, transportation, infrastructure, and other fields because of their excellent physical, chemical, mechanical, and technological properties. However, their susceptibility to corrosion is always an important factor limiting the safety and service life of metal equipment and facilities in service [1]. The failure of components caused by corrosion leads to safety accidents, environmental pollutions, and energy wastes [2]. Various nondestructive testing (NDT) technologies for the corrosion detection have been developed in recent years [3], [4], [5], [6]. As an important NDT technology, the ultrasonic

The associate editor coordinating the review of this manuscript and approving it for publication was Zhen Ren [ID].

method can detect subsurface corrosions, delaminations, cavities, cracks, and other defects in materials with high resolution [7], [8]. Compared to the traditional point-by-point sweeping ultrasonic NDT method, guided wave tomography (GWT) utilizes the dispersive properties of ultrasonic guided waves and requires only a small number of transducer arrays around the zone to be inspected, which can provide a good estimate of the remaining thickness of the corrosion spots. Owing to its advantages of a large detection range, high detection efficiency, and low detection cost in estimating the remaining thickness of corrosion defects, GWT has great potential application values for the quantitative determination of corrosion defects [9].

Common GWT algorithms mainly include ray tomography, diffraction tomography, and the full wave inversion

method [10]. The arrival time of guided-wave packets based on a ray model is used in the ray tomography method to reconstruct the slowness distribution. Although both straight and bent rays are used in the tomography process, this method is valid only when the defects are much larger than the wavelength of the guided wave because of the neglect of diffraction effects [11], [12]. The resolution of the diffraction tomography method can reach half of the wavelength, but its application prerequisites are that the defects should be of a limited size and the phase changes of the elastic waves passing through the defects are sufficiently small [13]. The combination of bent ray tomography and diffraction tomography methods improves the imaging resolution [14], [15], [16]. Compared with the above two tomography methods, the full waveform inversion (FWI) method makes full use of the frequency, phase, travel time, and amplitude information of the waveform, which is capable of explaining both transmitted and diffracted waves, and thus provides high-resolution imaging results [17], [18].

In recent years, the FWI method has been expanded from seismic exploration to biomedical engineering and industrial non-destructive testing. Related scholars completed the quantitative imaging of the acoustic velocity of the shin bone and the acoustic velocity and attenuation of breast tumor based on the single- and multi-parameter FWI methods [19], [20]. Rao et al. conducted a series of ultrasonic- GWT experiments on corroded metal plates. Combined with the dispersion characteristics of the guided wave, the residual thickness information of the corroded metal plates was inverted using the FWI method. The multi-parameter inversion capacity of the FWI method was also tested to simultaneously obtain the density and velocity information of metal parts. Those researches confirmed that, compared with other quantitative tomography methods, the resolution of imaging results based on the FWI method is significantly enhanced [21], [22], [23]. With its high-resolution capacity, the FWI method has been applied to the delamination inspection of concrete slabs [24], crack detection of turbine blades [10], and inclusions inspection of gears [25]. Nguyen et al. achieved high-resolution imaging results of small defects in complex heterogeneous structures by combining the FWI method with the reverse-time migration imaging method [26]. Ratassepp et al. [27] developed an efficient GWT method based on the FWI method for characterizing defects in anisotropic plates. The imaging results of the synthetic and experimental data show the good performance of the FWI method in determining the location, shape, and size of the defects in composite plates.

For the choice of forward modeling engine, FWI-GWT always exploits the 2D infinite-space acoustic approximation to efficiently simulate the wavefield. To mitigate the inaccuracies introduced by those approximations, the preprocess of observed signals is of great importance. During the FWI-GWT process, a number of emitting and receiving is carried out, formulating multiple channels of signal. A reference channel of signal, unaffected by the defect scattering effect, is often manually selected to design the matching filter which bridges the gap between the theoretical approximation and the actual observation [28]. The improper choice of reference channel leads to the decrease of imaging resolution and, more severely, the failure of the FWI process. The consequence is that those results may not be adequate for positioning and classifying defects. In addition, a relatively broadband spectrum is beneficial for FWI [29]. The low-frequency data are used for the estimation of a macro initial model, which helps FWI to converge towards the globally optimal model. The high-frequency data are subsequently used for refining the structural details, leading to the high-resolution imaging of defects. However, limited by the bandwidth of ultrasonic transducers, the selection of a high-frequency excitation band means the absence of low-frequency data, which may cause the failure of FWI-GWT when the targets defects are of complex and irregular distributions.

To address the above issues, a hybrid GWT method is proposed in this paper by combining ray tomography with FWI. The ray tomography method is first used to get a macro model, based on which the reference channel of signal for FWI can be automatically selected through the auto-calibration process. In addition, we use the imaging result (i.e., the macro model) of the ray tomography as the initial model for FWI, which increases the robustness of inversion by mitigating the issue of convergence towards local minimum. Therefore, we can exploit transducers with higher frequencies for obtaining images at a better resolution. Compared with the traditional FWI-GWT, the new method reduces the risk of errors that may be introduced by manual selection of reference signals. In addition, the new method reduces the nonlinear effects of the full-waveform inversion algorithm in the absence of low-frequency information for imaging complex defects. Compared with the traditional FWI algorithm, the hybrid method greatly improves the robustness of the algorithm and increases the imaging resolution. The rest of this study is structured as follows: the second section introduces the basic process of the hybrid GWT method; the third section is the application of the hybrid algorithm to simulated data; the fourth section presents the imaging results for the experimental data; and the fifth section provides conclusions and perspectives.

II. METHODS

The hybrid GWT process consists of three steps: ray tomography, auto-calibration of the measured data, and FWI imaging. The ultrasonic signals are first used as the input for ray tomography to obtain the macro imaging of the defects. After that, the selection of the reference signals is selected based on the macro imaging result in an automatic manner. Accordingly, we calculate the calibration factors to process the observed ultrasonic signals channel-by-channel. Next, we input the macro model and calibrated data to FWI for iteratively updating the parametric model. When the misfit function reaches the convergence condition, we obtain
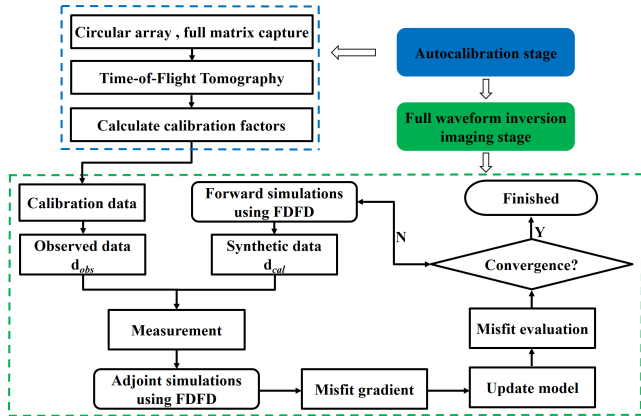
FIGURE 1. Flow diagram of the auto-calibration GWT algorithm based on FWI.

the residual thickness map by transforming inverted phase velocity to structure thickness. The flow diagram of the hybrid algorithm is illustrated in Figure 1.

A. AUTO-CALIBRATION METHOD

In the GWT method based on FWI, to improve the inversion efficiency, the forward modeling is usually based on the acoustic wave equation approximation. But the experimental data or finite element simulation data are elastic modeling. The calibration factors need to be introduced to reduce the bias existing between the approximation and actual models [21]. The calibration factors are expressed as follows:

$$\text{cali} = \frac{\text{fft}(\psi_0)}{\text{fft}(d_{obs,0})} \quad (1)$$

where $d_{\text{obs},0}$ represents the actual observation data received from the emitter-receiver path that is not affected by the defects. ψ_0 denotes the modeling waveforms using the acoustic wave equation in a homogeneous model without defects. fft() denotes the fast Fourier transform.

During the imaging process, we prefer not to select the channel, associated with waves affected by defect, as the reference. An improper choice of reference channel not only introduces strong artifacts to the imaging results but also leads to the failure of the imaging process in severe cases. In this paper, we derive the automatic selection of the reference signal and the calculation of the calibration factor following the approach of Druet [28] who proposed a hybrid tomography algorithm by combining the ray and diffraction tomography methods. Taking an aluminum plate as an example, the data-processing flow of the auto-calibration method is given in the following.

Figure 2(a) shows the original thickness map of the aluminum plate. There is a circle defect (50 mm in diameter) in the center of the plate. A circle array with 30 transducers (red points in Figure 2(b)) is assembled around the defect. The ray paths for all emitter-to-receiver pairs are shown as light blue lines in Figure 2(b). The observation data in (1) for all ray paths are simulated by the finite element method.
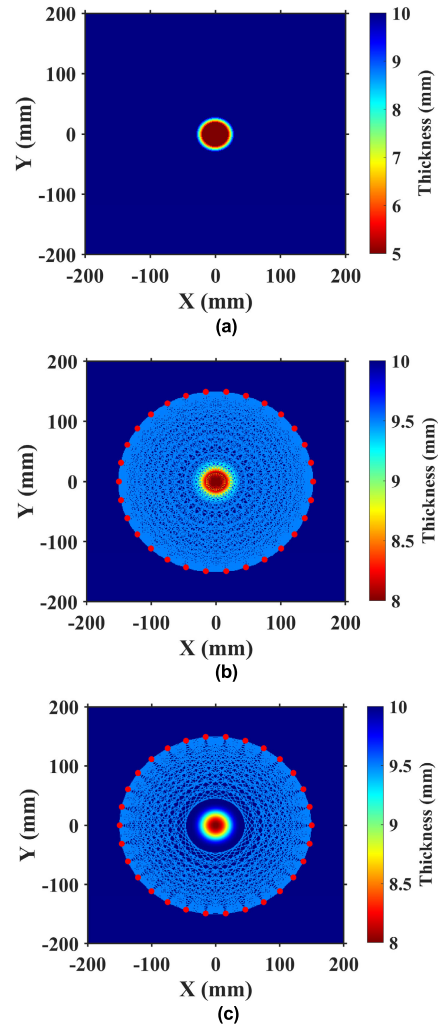

FIGURE 2. Selection of emitter-to-receiver paths based on the ray tomography result for the models with central defect. (a) Original thickness map with central defect. (b) Ray paths for all emitter-to-receiver pairs. (c) Ray paths in healthy area picked out by the threshold method.

The synthetic data are first used to perform the straight-ray GWT. The imaging result is shown as the background of Figure 2(b) (removing the transducers and ray paths). Based on the imaging result, for each ray path, a threshold of the ratio of the inversion thicknesses to the background thickness can be set to determine whether the ray path passes through the defects. given in the following. Let the total number of rays be n_{rays}, the number of transducers be n_{sensors}, and the ray paths without passing through defects be m, then $n_{\text{rays}} = n_{\text{sensors}}(n_{\text{sensors}} - 1)$ and $m \leq n_{\text{rays}}$. In this paper, the threshold is set to be 3%. Thus, the reference signals do not pass through the defects are picked out. The rays which do not pass through the defects are shown in Figure 2(c).

As noticed before, the ray tomography algorithm is blind to the diffraction effect, which means that the rays picked out in Figure 2(c) have a certain chance of being influenced by the defects. To explain the influence of the diffraction
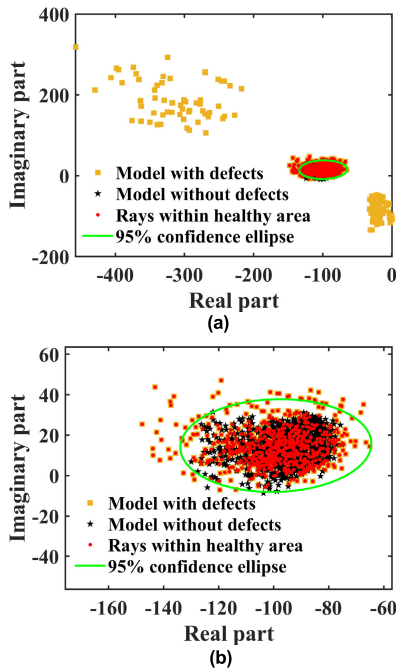
FIGURE 3. The distribution characteristics of calibration factors for the models with central defect or not. (b) is the partial enlargement of (a). The black pentagram and yellow square scatters respectively represent the calibration factors for the models with central defects or not. The red round scatters represent the calibration factors of the ray paths in healthy area picked out by the threshold method. The green ellipse denotes the 95% confidence ellipse of the red round scatters.

effect, the observation data for the model without defects are also modeled using the finite element method. The measuring parameters are the same as the model in Fig 2. The acoustic approximation modeling waveforms without defects in (1) are modeled using the finite-difference method. We calculated the calibration factors for the finite element simulation model with defects. The calibration factors at a certain frequency are plotted on the complex plane. The calibration factors for the corresponding source-receiver pairs in Figure 2(b) are plotted as shown in the yellow squares in Fig. 3. The calibration factors for the corresponding source-receiver pairs in Figure 2(c) are plotted as shown in the red round scatters in Fig. 3. Similarly, we calculated the calibration factors for the finite element simulation model without defects as shown the black pentagrams in Fig. 3. Finally, we selected 95% confidence ellipses for all red round scatters (shown as green solid lines). Figure 3(b) is the partial enlargement of Figure 3(a). The calibration factors of the model without defects (black pentagram scatters) distribute comparatively centralized, which are much closed with the red round scatters (the calibration factors of the ray paths in healthy area picked out by the above threshold method) in Figure 3. The rest of the yellow square scatters represents the calibration factors of the ray paths that directly pass through the defects, which significantly stay away from the calibration factors within the healthy area.

From Figure 3(b), we can see that the distribution area of the red round scatters is slightly larger than the black pentagrams, which may be caused by the influence of the diffraction effect. Therefore, to exclude paths that may be affected by the scattering effect of defects, a 95% confidence ellipse (green ellipse in Figure 3) is calculated based on the distribution of the calibration factors (red scatters) within the healthy area. After this filtering process, only q ($q < m$) factors (red scatters in green ellipse) remained. Let those q calibration factors be c^{ellipse}, which satisfy $c^{\text{ellipse}} \in \mathbb{C}^q \subset \mathbb{C}^{n_{\text{rays}}}$. Finally, the calibration factors c^{defect} outside the ellipse are replaced by the average of the calibration factors inside the ellipse ($c^{\text{defect}} = \sum_{k=1}^{q} c_k^{\text{ellipse}}/q$), while the calibration factors inside the ellipse remain unchanged. For synthetic data, selecting a more stringent region does not have a significant influence on the imaging results. However, in actual data processing, the confidence region should be selected based on the noise level.

B. FULL WAVEFORM INVERSION
In general, FWI method mainly consists of two parts: the forward modeling to generate synthetic data and the inverse process to update the model by calculating the gradient of the misfit function.

1) FORWARD MODELING FOR ULTRASONIC WAVE PROPAGATION
To improve the efficiency of FWI, the scalar acoustic wave equation is usually used to approximate the propagation of guided waves in solid media. The form of the two-dimensional acoustic wave equation in the frequency domain can be written as

$$(\nabla^2 + \omega^2 m^2)\psi(r, \omega) = -s(r, \omega) \qquad (2)$$

where $\nabla^2 = \frac{\partial}{\partial x^2} + \frac{\partial}{\partial y^2} = \partial_x^2 + \partial_y^2$ is the Laplace operator; $r(x, y)$ is the spatial position in the Cartesian coordinate system. ω is the angular frequency; $m = 1/c$ is the slowness of acoustic wave; c is the acoustic wave velocity. $\psi(r, \omega)$ is the displacement field; $s(r, \omega) = s(\omega)\delta(r - r_s)$ denotes the source signal; $s(\omega)$ is the Fourier transform of the source signal; $\delta(r - r_s)$ denotes the Dirac function; r_s denotes the source position.

The finite difference method [30] is used in the forward simulation process to solve the partial differential equations. A perfect matching layer (PML) is added around the computational region to reduce the computational cost and the influence of reflected waves by the edges of the computational region. Using the finite difference discretization, (3) can be expressed as

$$A\psi = s \qquad (3)$$

where $A = \nabla^2 + \omega^2 m^2$ is the complex-value impedance matrix, which depends on frequency, material properties, discrete format, and boundary conditions. The impedance

matrix A is a $l \times l$ matrix. $\boldsymbol{\psi}$ and $\boldsymbol{s}$ respectively represents the pressure wave-field and source term, which are all $l \times 1$ vectors.

To reduce the computational cost, the LU factorization can be used to solve the wave field $\boldsymbol{\psi}$:

$$LU\boldsymbol{\psi} = \boldsymbol{s} \qquad (4)$$

where $\boldsymbol{L}$ and $\boldsymbol{U}$ respectively denote the upper and lower triangular matrix from the LU factorization. The factored matrix A can be used to solve the forward problem of other source vectors, thus speeding up the computation process.

2) INVERSE THEORY

A least-square norm of the data residuals between the synthetic and observed data is chosen as the object function,

$$E(\boldsymbol{m}) = \frac{1}{2}\|P_r(\boldsymbol{\psi}) - \boldsymbol{d}\|^2 = \frac{1}{2}\left(\Delta\boldsymbol{d}^t\right)^* \Delta\boldsymbol{d} \qquad (5)$$

where $\boldsymbol{m} = [m_1, m_2, \ldots, m_{n_x n_y}]^T$ is the parameters of the forward model. P_r is the sampling operator of the wave field at the receiver position in the forward model. $\boldsymbol{\psi} = \{\psi_i\}$ and $\boldsymbol{d} = \{d_i\}, i = (1, 2, \ldots n_r)$ respectively denote the vectors of synthetic data and observed data. $\Delta\boldsymbol{d} = \sum_{i=1}^{n_r}\{p_r(\psi_i) - d_i\}, i = (1, 2, \ldots, n_r)$ is the data residual (difference between data $p_r(\psi_i)$ calculated using the current model $\boldsymbol{m}$ and the observed data d_i). The superscript t and $*$ denote the transposition and complex conjugate of vector or matrix, respectively.

Based on Taylor's theorem, we have

$$E(\boldsymbol{m} + \delta\boldsymbol{m}) \approx E(\boldsymbol{m}) + \boldsymbol{g} \cdot \delta\boldsymbol{m} + \frac{1}{2}\delta\boldsymbol{m}^t \cdot \boldsymbol{H} \cdot \delta\boldsymbol{m} = p\left(\delta\boldsymbol{m}\right) \qquad (6)$$

where $g = \partial E(m)/\partial m = \Re e(\boldsymbol{J}^t \Delta d^*)$ is the gradient vector; $\boldsymbol{J} = \partial\psi_p\left(m_q\right)/\partial m_q, p = (1, 2, \ldots, n_r), q = \left(1, 2, \ldots, n_x \times n_y\right)$ is the Fréchet derivative matrix, and $\Re e$ denotes the real part of the complex values. $\boldsymbol{H} = \frac{\partial^2 E(\boldsymbol{m})}{\partial\boldsymbol{m}^2}$ denotes the Hessian matrix. To minimize the object function $E(\boldsymbol{m})$, let $\frac{dP(\delta\boldsymbol{m})}{d(\delta\boldsymbol{m})} = \boldsymbol{g} + \boldsymbol{H}\delta\boldsymbol{m}$ be zero then $\delta\boldsymbol{m} = -\boldsymbol{H}^{-1} \cdot \boldsymbol{g}$. Therefore, the model can be updated as

$$\boldsymbol{m}_{k+1} = \boldsymbol{m}_k - \varepsilon\boldsymbol{H}^{-1}\boldsymbol{g} \qquad (7)$$

where ε denotes the step size. When only the first-order derivative of the Hessian matrix is considered, the corresponding method is the fastest descent method whose implement process is relatively simple. This is a straight-forward method, but its slow convergence rate limits its application to large-scale problems. To boost the convergence rate, the second-order derivative Hessian matrix should be considered. However, the computational cost and the storage space required for computing the inverse Hessian matrix increase sharply. To avoid the direct computation of the inverse of the Hessian matrix, the limited-memory Broyden–Fletcher–Goldfarb–Shanno (L-BFGS) method [31] that can

approximately calculate the inverse of the Hessian matrix was used in this study.

The convergence criterion Q is defined as:

$$Q^{(n)} = \frac{\iint \left|d^n(x, y) - d^{n-1}(x, y)\right| dxdy}{\iint d_{\text{health}}dxdy} \qquad (8)$$

where d_{health} represents the thickness of the plate without defects; $d^n(x, y)$ denotes the thickness at the position (x, y) in the n-th iteration. In this study, the iterative process is terminated when $Q \leq 2 \times 10^{-4}$. Moreover, to avoid the iteration falling into an infinite loop, when the loop count is larger than M, the iteration algorithm will stop and the convergence criterion is considered to be reached. Based on experience, the loop count M was chosen to be 30.

To quantize the quality of the imaging results, the global relative error E_{global} is defined as:

$$E_{\text{global}} = \frac{\left\|\tilde{\boldsymbol{d}} - \boldsymbol{d}\right\|_2}{\left\|\tilde{\boldsymbol{d}}\right\|_2} \qquad (9)$$

where $\tilde{\boldsymbol{d}}$ and $\boldsymbol{d}$ respectively denote the actual and inverted thicknesses of the plate.

3) REGULARIZATION METHOD

In the actual imaging process, because of the influence of experimental error or the shortcomings of the imaging algorithm, some noise or artifacts are inevitably generated in the imaging results. The Gaussian filtering method is often used in the iterative imaging process to reduce the impact of the noise and artifacts and increase the imaging accuracy. The standard deviation of the Gaussian filter directly depends on the resolution of the tomography algorithm. The resolution of the ray tomography algorithm is $\sqrt{L\lambda}$, where L is the distance between the transmitting and receiving transducers and λ is the wavelength. The resolution of the FWI algorithm based on the elastic model is 1.5~2 wavelengths [32]. Based on some test results, the standard deviation for ray and FWI algorithms are respectively set as 1 and 0.5 wavelengths in this study.

The auto-calibration process in section II-A is highly susceptible to the noise in the ray tomography imaging results. In addition to Gaussian filtering, we also applied threshold regularization and variable relaxation regularization to eliminate imaging noise [28]. The threshold regularization method is based on the fundamental assumption that corrosion only reduces the plate thickness, so that the inverted thickness values greater than the background thickness are set as the background thickness. The variable relaxation regularization method, which is derived from the Tikhonov normalization method, can accurately reconstruct local defects above the noise threshold at the expense of the low sensitivity to small defects. The inverted thickness d'_{ij} after the variable relaxation
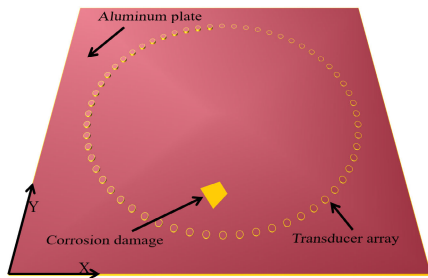
FIGURE 4. The geometric diagram of the simulation model.

regularization method can be written as:

$$
d'_{ij} = \begin{cases} \tilde{d} + \dfrac{d_{ij} - \tilde{d}}{(1 + \frac{1}{z_{ij}^2})^{\frac{\alpha}{2}}} & 0 < \left| d_{ij} - \tilde{d} \right| < \gamma\beta\tilde{d} \\ d_{ij} & \text{others} \end{cases}
$$

$$
z_{ij} = \begin{cases} \dfrac{\left| d_{ij} - \tilde{d} \right|}{\beta\tilde{d}} & \left| d_{ij} - \tilde{d} \right| < \beta\tilde{d} \\ \dfrac{\left| d_{ij} - \tilde{d} \right|}{0.5\beta\left[1 - \cos(\pi\frac{\left| d_{ij}-\tilde{d} \right| - \gamma\beta\tilde{d}}{(1-\gamma)\beta\tilde{d}}) \right]} & \\ \beta\tilde{d} \le \left| d_{ij} - \tilde{d} \right| < \gamma\beta\tilde{d} \end{cases} \tag{10}
$$

where $\tilde{d}$ is the reference value for regularization, which is generally set to the original thickness of the plate; d_{ij} denotes the inverted thickness of the ray tomography method. $\alpha \in \mathbb{R}_+$ is a constant that defines the regularization strength. The higher the value of the parameter, the deeper the defect will be set to the background thickness. $\beta \in [0, 1]$ is a fixed value that depends on image noise. The higher the value of the parameter, the lower the background noise after regularization; $\gamma \in [1, +\infty)$ is the fixed relaxation constant. The product of γ and β determines the influence range of the regularization method on the thickness, the higher the value of the product, the deeper the defect will be affected. In the actual imaging process these three parameters need to be set to the appropriate value, the higher the value of the parameters, the lower the imaging noise, but the greater the imaging error. However, if the value of the parameters is too low, there will be a lot of imaging noise, causing problems for the auto-calibration process. More information of the influence of these parameters on the imaging results can be seen in [28]. In this study, the regularization parameters are set as $\alpha = 4$, $\beta = 0.1$, and $\gamma = 10$.

III. NUMERICAL TESTS

Figure 4 shows the numerical simulation model, a 10-mm-thick aluminum plate with defects (density is 2700 kg/m3, elastic modulus is 70 GPa, and Poisson's ratio is 0.33). A circle array with 30 transducers was assembled on the surface of the plate. The diameter of the circle array was 300 mm. The numerical simulations of the propagation
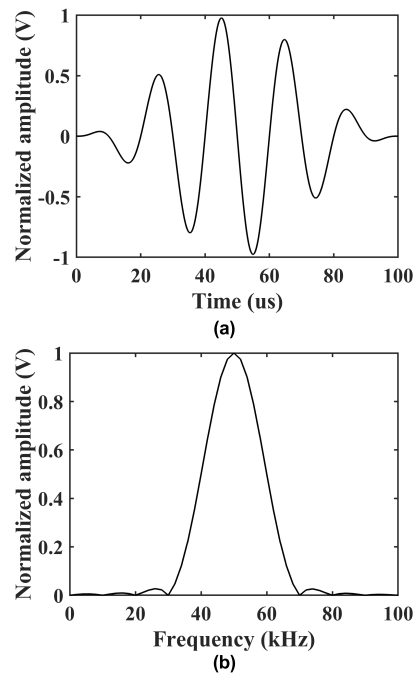

FIGURE 5. Source signal used in the simulation process. (a) Excitation signal of the 5-cycle Hann-windowed tone-burst signal with a center frequency of 50 kHz. (b) Its corresponding frequency spectrum.

of the three- dimensional elastic waves were performed using the finite element method. To excite a relatively pure A0 mode, an out-of-plate displacement source was applied to the emitter transducer. The source function was a 5-cycle Hann-windowed tone-burst signal whose central frequency is 50 kHz, with a bandwidth of approximately 15 dB from 35 to 65 kHz (as shown in Figure 5). In the simulation process, one transducer was an emitter and the other 29 transducers were receivers. Repeating this operation up to all the transducers have acted as an emitter and a 30 × 29 signal data matrix would be obtained. To investigate the ability of the auto-calibration method to identify defects located at different positions, two data matrixes were simulated on the model in Figure 4 with defects located in the center of the circle array or not.

A. CENTRAL DEFECT

Figure 6(a) displays the thickness map of the plate with a defect located at the center of the circle array. The defect is shown as a trapezoidal cylindrical alcove whose top and bottom diameters are respectively 60 and 40 mm. The cross-section thickness distribution located at Y = 0 mm (the white dashed line in Figure 6(a)) is shown as the solid black line in Figure 6(c). The synthetic data matrix was first calibrated according to the auto-calibration method and the results of the calibration process are shown in section II-A. The data matrix after calibration is used for the FWI process. The inversion process is performed with a moving frequency from 35 kHz to 60 kHz to mitigate the nonlinearity of the inversion problem. The 60 kHz imaging result of GWT based
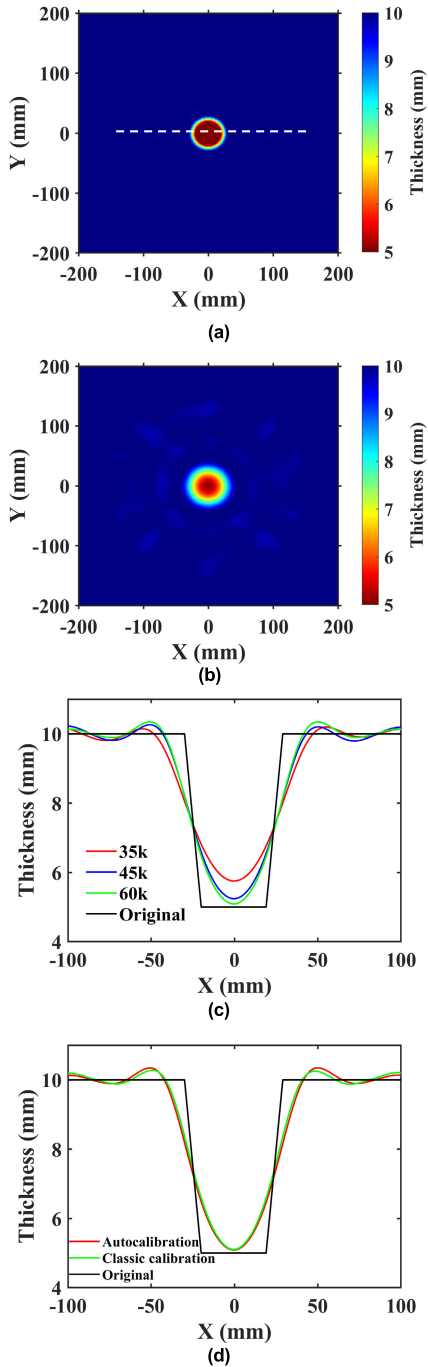
FIGURE 6. Inverted thickness distribution maps for the model with central defect. (a) Original thickness map. The white dashed line marks the position to extract the cross-section thickness distribution maps in (c) and (d). (b) The thickness distribution maps inverted by the auto-calibration method. (c) The successive-frequency inversion results of the cross-section in (a) at 35, 45, and 60 kHz. (d) The inversion results by the auto-calibration method and the classical method.

TABLE 1. Global relative error eglobal by classical calibration and auto calibration methods (synthetic data).

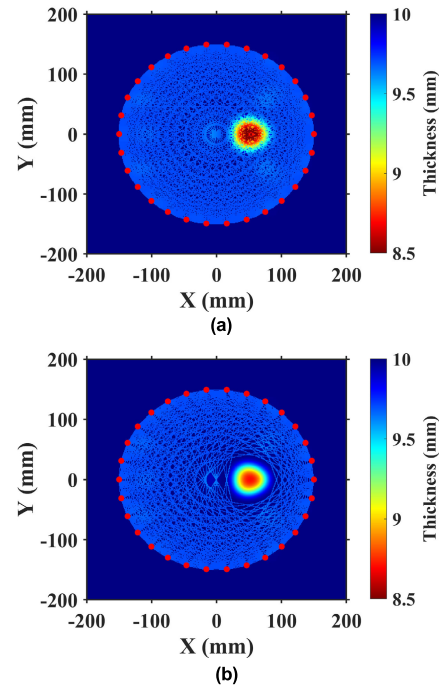|	Central defect	Eccentric defect
Classic calibration	1.52%	0.90%
Auto-calibration	1.39%	0.87%

FIGURE 7. Selection of emitter-to-receiver paths based on the ray tomography result for the models with eccentricity defect. (a) Ray paths for all emitter-to-receiver pairs. (b) Ray paths in healthy area picked out by the threshold method.

distributions of the inversion results in the successive-frequency process. The cross-section thickness distributions at Y = 0 mm at 35 kHz, 45 kHz and 60 kHz are shown in Figure 6(c). From the comparison, we can see that the higher the frequency, the smaller reconstruction error for the deepest defects. The minimum error at the center of the defects is 0.08mm. Figure 6(d) shows a comparison between the classical method (artificially selecting one available reference signal) and the auto-calibration method for the thickness distributions at Y = 0 mm. Although the thickness distribution of the auto-calibration method at 60 kHz is essentially the same as the classical method, the global error of the auto-calibration method is slightly smaller than the classical method (shown in Table 1).

B. ECCENTRICITY DEFECT
In this section, the same trapezoidal cylindrical alcove defect in section III-A is located 50 mm to the right of the center of the circle array. Similar to the process in section III-A, the synthetic data matrix is first used as the input of the ray tomography algorithm. The imaging result
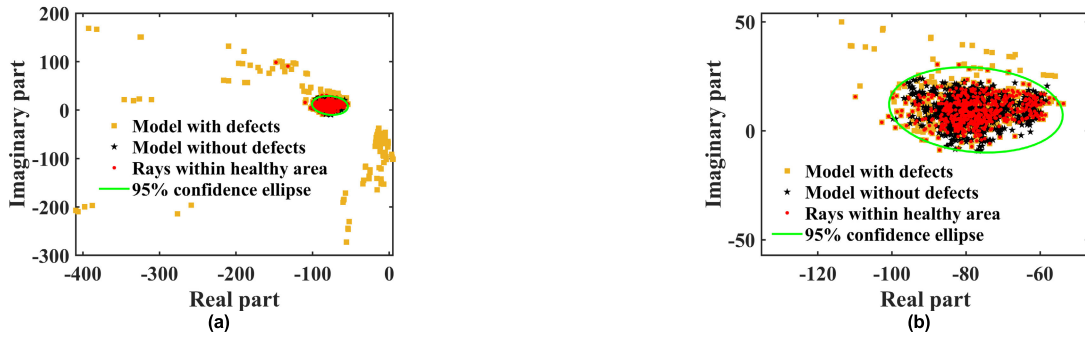
on the successive-frequency inversion method is shown in Figure 6(b). Although there are some faintly discernible artifacts in the imaging zone, the shape and outline of the defects are well inverted. To further display the details of the imaging result, we extract the cross-section thickness

FIGURE 8. The distribution characteristics of calibration factors for the models with eccentricity defect or not. (b) is the partial enlargement of (a). The black pentagram and yellow square scatters respectively represent the calibration factors for the models with central defects or not. The red round scatters represent the calibration factors of the ray paths in healthy area picked out by the threshold method. The green ellipse denotes the 95% confidence ellipse of the red round scatters.
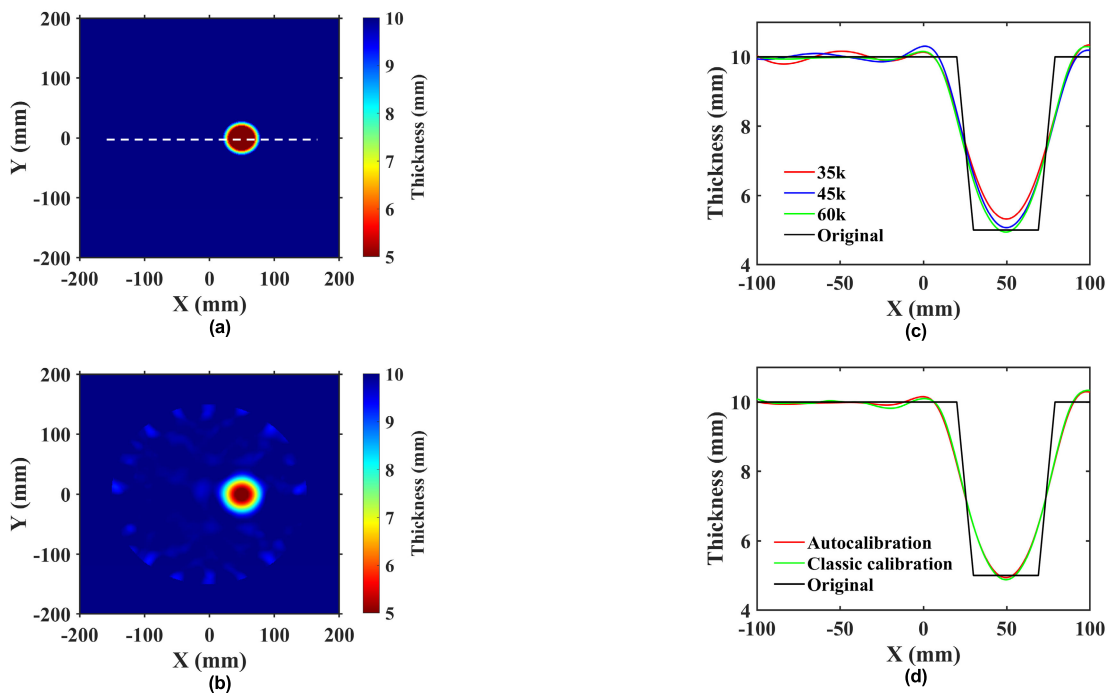

FIGURE 9. Inverted thickness distribution maps for the model with the eccentricity defect. (a) Original thickness map. The white dashed line marks the position to extract the cross-section thickness distribution maps in (c) and (d). (b) The thickness distribution maps inverted by the auto-calibration method. (c) The successive-frequency inversion results of the cross-section in (a) at 35, 45, and 60 kHz. (d) The inversion results by the auto-calibration method and the classical method.

reconstructed by the straight-ray tomography is shown in Figure 7(a). The red points in Figure 7(b) represent transduces of the circle array. The light blue lines denote all transmit-receive paths. The selected ray paths that do not pass through the defect zone by the threshold method is shown in Figure 7(b).

Similar to the case of a central defect, most of calibration factors of the ray paths in Figure 7(b) (red round scatters in Figure 8(a)) have a comparatively centralized distribution, which are much closed to the calibration factors of the model without defects (black pentagram scatters in Figure 8(a)). The calibration factors of the ray paths passing through the defects are further away from the distribution of the black pentagram scatters. Although there are only a little of the red round

scatters are further away from the central area due to the loss of the symmetrical properties of the defect, the calibration process can also be completed by selecting a 95% confidence ellipse of the red round scatters in Figure 8 and substituting the calibration factors out of the confidence ellipse by the mean of the factors in the ellipse. Figure 9(a) and 9(b) respectively display the original model and the imaging result of FWI with auto-calibration. The cross-section thickness distributions at Y = 0 mm of the successive-frequency inversion method is shown in Figure 9(c). The cross-section thickness distributions of the auto-calibration and classical calibration methods are compared in Figure 9(d). Similar to the imaging result in section III-A, the auto-calibration method can get the quite accuracy with the classical method
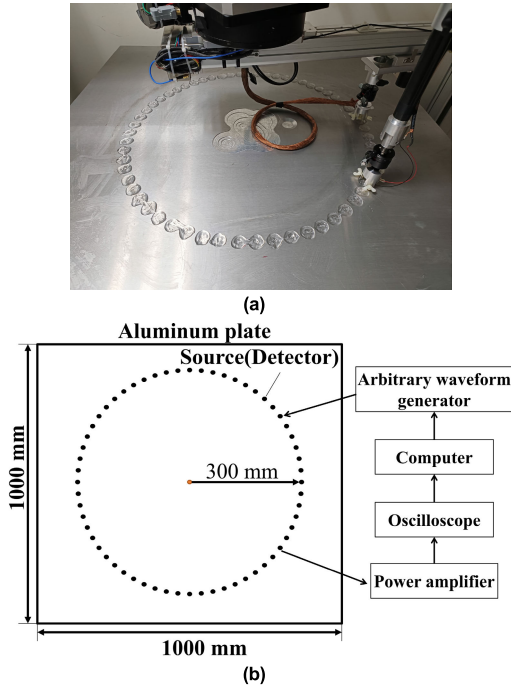
(a)

(b)

FIGURE 10. Schematic diagram of the experimental procedure. (a) The 10 mm thick aluminum plate with double defects. (b) Measuring equipments and process.

FIGURE 11. Lamb wave dispersion curves for a 10-mm-thick aluminum plate.

(a)

(b)

FIGURE 12. Experimental waveform data received by one receiver. (a) Time-domain waveform data. The back line represents the original waveform. The red line represents the time-window function. The blue line denotes the direct A0 mode waveform extracted from the original waveform. (b) Spectral magnitude of the direct A0 mode wave.

and its global error is slightly smaller than the classical method.

IV. EXPERIMENTAL TESTS

To test the performance of the new algorithm, we conducted experiments on a 6061-type aluminum plate. The dimensions of the plate are $1000 \times 1000 \times 10$ mm (density is 2700 kg/m3, elastic modulus is 70 GPa, and Poisson's ratio is 0.33). The schematic diagram of experiment is shown in Figure 10. A 5-cycle Hann-windowed tone-burst signal with center frequencies 50 kHz and 70 kHz were respectively used as the exciting signal. The received signals were amplified by the pre-amplifier and recorded by the oscilloscope. Two piezoelectric transducers (diameter is 10 mm and the center frequency is 50 kHz) were respectively assembled on two mechanical arms with the same center and turning radius (shown in Figure 10(a)). According to Rao J [21], the minimum number of transducers in a circular array to correctly sample the wave-field can be expressed as $N > 4\pi r/\lambda$ where r denotes the radius of the transducer arrangement and λ denotes the wavelength. At 80 kHz ($\lambda = 30.1$ mm), around 125 transducers would be needed to correctly reconstruct the image for an area of 300 mm in radius. However, it is not practical to have too many transducers in the experiment and therefore the number of transducers is limited to 60 in this study. One was emitter transducer and the other was receiver transducer. In the data acquisition process, the position of the emitter transducer kept unchanged and the receiver transducer rotated every
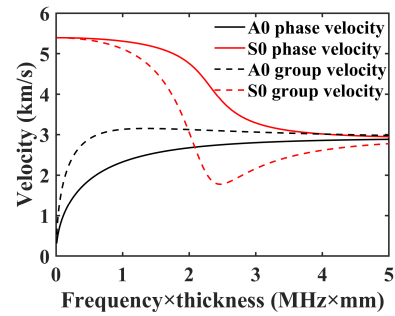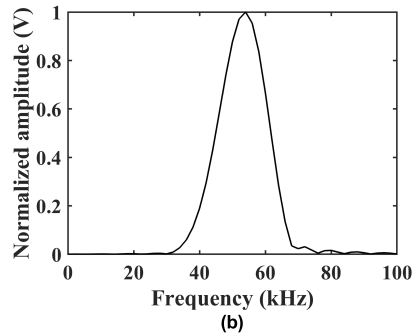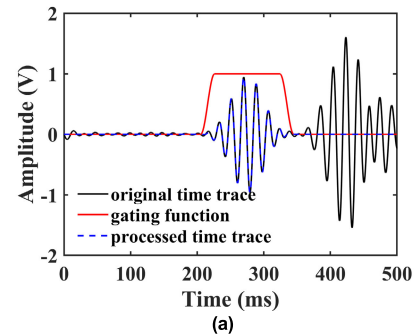
six degrees and recorded data. When all the data of the receiver position were recorded, the emitter rotated six degrees. Repeating the above process, the data matrix by the virtual ring array (displayed in Figure 10(b)) was recorded. The radius of the virtual ring array was 300 mm. Due to the limitation of the fixture, a few receiver points close to the source could not be acquired. The nearest central angle of the transmitter-to-receiver was 18 degrees and a 60×55 data matrix was recorded.

As shown in Figure 11 and 12, high-quality A0-mode Lamb waves were generated, followed by the reflection waves of the plate edges. In this paper, only the first arrival A0-mode waves are used for the GWT. The band-pass filtering and time window method were used to extract the required A0 mode. The pre-processing result of one channel
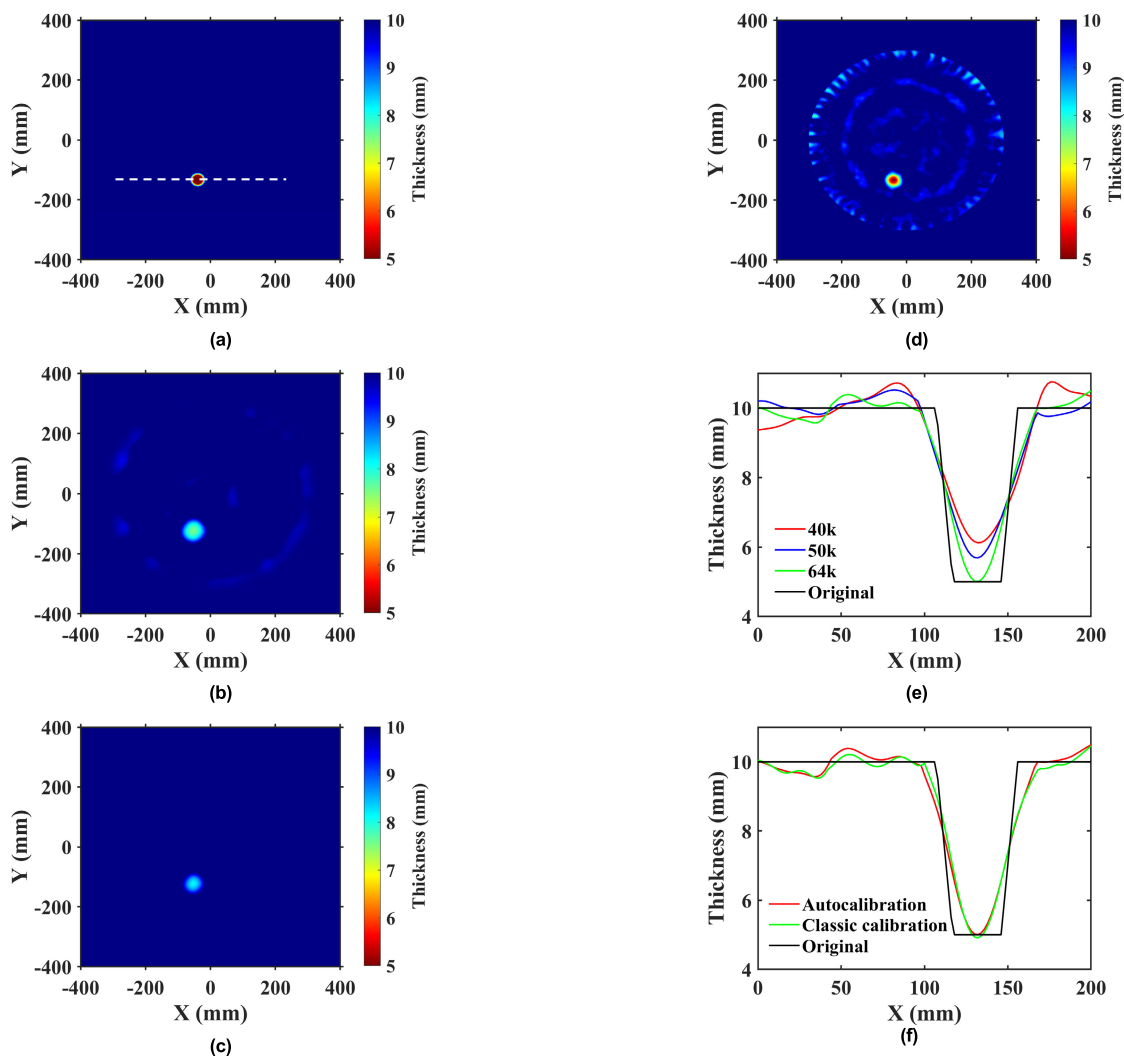
FIGURE 13. Inverted thickness distribution maps for the experimental model with eccentricity defect. (a) Original thickness map. The white dashed line marks the position to extract the cross-section thickness distribution maps in (e) and (f). (b) The thickness distribution maps inverted by the ray tomography. (c) The regularization result of (b). (d) The thickness distribution maps inverted by the auto-calibration method. (e) The successive-frequency inversion results of the cross-section in (a) at 40, 50, and 64 kHz. (f) The inversion result by the auto-calibration method and the classical method.

waveform data is shown as the blue line in Figure 12(a). After extracting the desired mode waves, the signal envelopes were obtained using the Hilbert transform, and 50% of the envelope peaks were taken as the travel time of A0 mode to perform the straight-ray tomography algorithm. Similar to the process of synthetic data in section III, the imaging results of different experimental models are displayed in the following section.

A. SINGLE DEFECT
Figure 13(a) shows the thickness map of the aluminum plate with a defect machined by the CNC milling system. The defect is shown as a trapezoidal cylindrical alcove whose top and bottom diameters are respectively 50 and 30 mm. The center of the defect is located at (−40 mm, −132 mm). The experimental data was first used to perform the straight-ray

tomography algorithm and the inverted thickness map is shown in Figure 13(b). The imaging result inevitably has a certain amount of noise and artifacts, which is detrimental to the auto-calibration process. Hence, the threshold regularization and variable relaxation regularization methods were used to reduce the negative effect of the artifacts and the result are shown in Figure 13(c). From the comparison of Figure 13(b) and 13(c), we can see that the noises and artifacts have greatly decreased. The imaging result of GWT based on the successive-frequency FWI inversion method is shown in Figure 13(d). Although the noises and artifacts of the imaging results are slightly larger than the synthetic data in section III, the shape and outline of the defect are well inverted. The cross-section thickness distributions at Y = −132 mm for different frequencies are shown in Figure 13(e). With the frequency increasing, imaging accuracy gradually
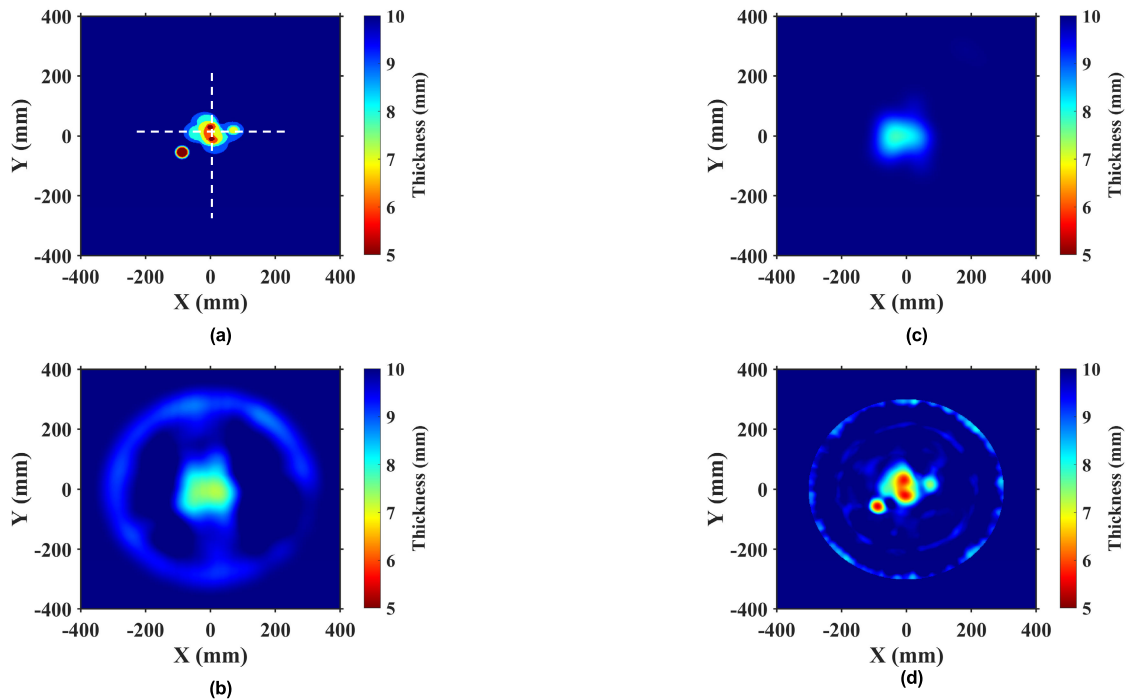
FIGURE 14. Inverted thickness distribution maps for the experimental model with double defects. (a) Original thickness map. The white dashed line marks the position to extract the cross-section thickness distribution maps in Figure 15. (b) The thickness distribution maps inverted by the ray tomography. (c) The regularization result of (b). (d) The thickness distribution maps inverted by the auto-calibration method.
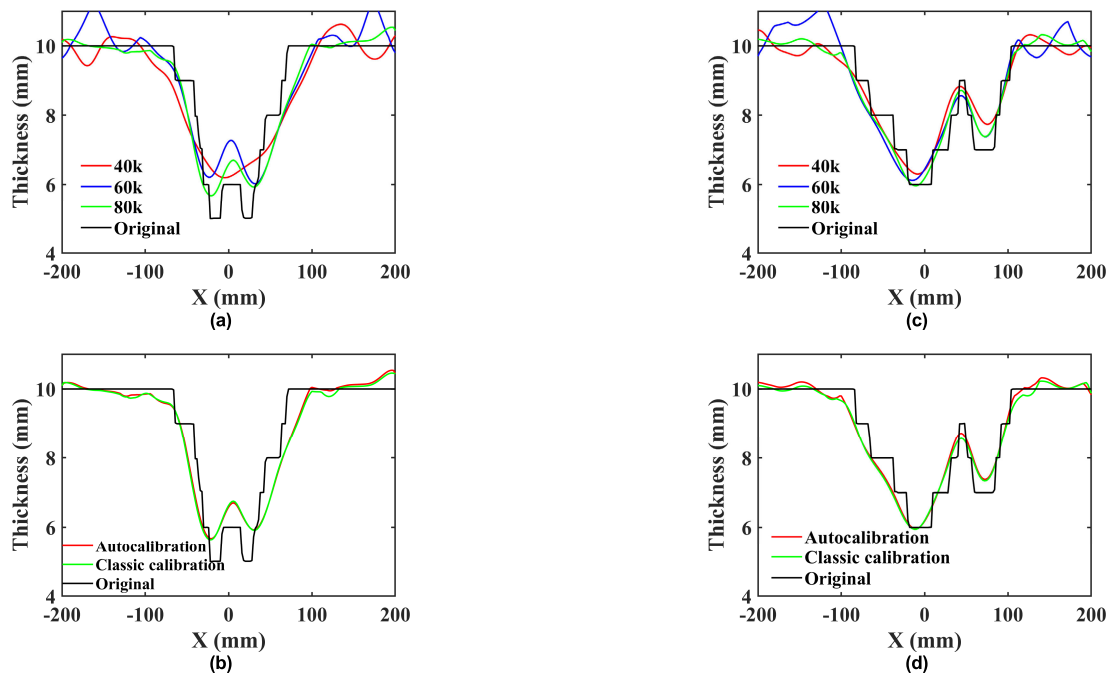

FIGURE 15. The cross-section thickness distribution maps for the experimental model with double defects along the white dash line in Figure 14(a). The successive-frequency inversion results along the (a) vertical and (c) horizontal white dash line at 40, 60, and 80 kHz. The inversion results along the (b) vertical and (d) horizontal white dash line by the auto-calibration method and the classical method.
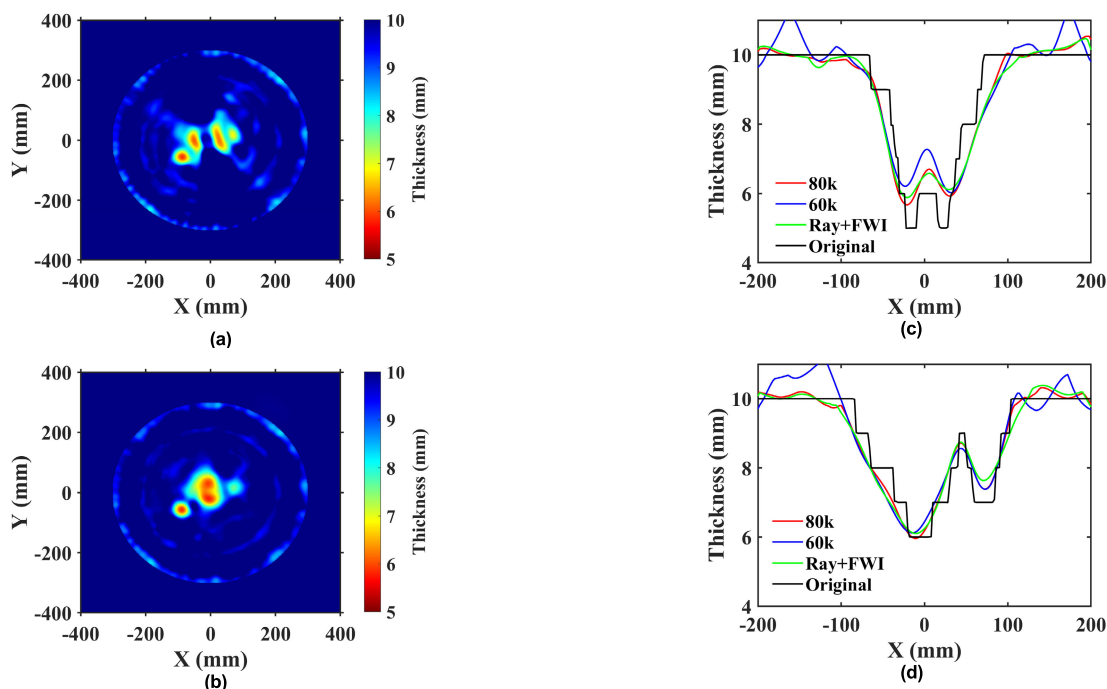

FIGURE 16. Inverted thickness distribution maps for the experimental model with double defects when the low-frequency data absence. Thickness map inverted by the (a) classical method and (b) the auto calibration method. The inversion results along the (c) vertical and (d) horizontal white dash line in Figure 14(a). The red and blue lines represent the inverted result by the auto-calibration method at 60 and 80 kHz using both the low- and high- frequency data. The green line denotes the inversion results by the auto-calibration method using the high-frequency data only.

TABLE 2. Global relative error eglobal by classical calibration and auto-calibration methods (experimental data).

	Single defect	double defect
Classic calibration	1.16%	1.74%
Auto-calibration	1.05%	1.65%

improves. At the highest frequency (64 kHz), only 0.01 mm is underestimated at the center of the defect. Figure 13(f) shows the reconstructed cross-section thickness distributions using the auto-calibration and classical methods. In the case of the experimental data, the FWI based on the auto-calibration method has better reconstruction accuracy. The global relative error at 64 kHz of the auto-calibration method for a single defect is slightly smaller than that of the classical method (shown in Table 2).

B. DOUBLE DEFECTS

Figure 14(a) displays the thickness map of the aluminum plate with double defects. Compared with Figure 13(a), an irregular defect was machined by the CNC milling system. To get relatively broadband signals, the experimental data with different exciting frequencies were recorded. The center frequencies of the exciting signal were 50 kHz and 70 kHz, respectively. The thickness map inverted by the straight-ray tomography with double defects is shown in Figure 14(b). The result processed by the threshold regularization and variable relaxation regularization methods is shown in

Figure 14(c). The experimental data were automatically calibrated and then inverted sequentially from low to high frequencies at five frequencies of 40, 50, 60, 70, and 80 kHz. The inversion result at 80 kHz is shown in Figure 14(d). The cross-section thickness distributions at X = 4 mm (the white vertical dashed line in Figure 14(a)) in different frequencies is shown in Figure 15(a). The cross-section thickness distributions at Y = 20 mm (the white horizontal dashed line in Figure 14(a)) in different frequencies is shown in Figure 15(c). It can be seen that the reconstruction error for the defects gradually decreased as the frequency increased. The comparison of the cross-section thickness distributions using the classical and auto-calibration method is shown in Figure 15(b) and 15(d), respectively. Although the 5 mm defect cannot be well reconstructed due to the increased complexity of the defects, compared to the classical method, our auto-calibration method is still able to guarantee a slightly smaller global error (Table 2).

C. IMAGING RESULTS FOR LOW-FREQUENCY ABSENCE DATA

In the actual imaging process based on FWI, a relatively broadband data is needed for the meticulous depiction of the irregular and intricate defects. The high-frequency data represents the high wave number information of the model, which depicts the influence of the small-scale perturbation quantity of the defect. This greatly increases the nonlinearity

TABLE 3. Global relative error eglobal by the auto-calibration method using both low- and high- frequency data and using low-frequency data only. (experimental data).

	double defect
Ray+FWI	1.68%
Auto-calibration (60k)	1.83%
Auto-calibration (80k)	1.65%

of the inverse problem, so the low-frequency data is used to provide a macro initial model to ensure the conduct of FWI. From the above imaging results of synthetic and experimental data, we can also find that the higher the frequency, the smaller the reconstruction error for the defects. However, limited by the bandwidth of the ultrasonic transducer, twice data records with different exciting frequencies like that in section IV-B, will sharply decrease the efficiency of nondestructive testing. To improve the imaging accuracy as much as possible, high-frequency exciting means the absence of low-frequency data. This will bring a great challenge for the FWI method, especially for the irregular and intricate defects in the actual nondestructive testing. This is because the absence of low-frequency data means the macro initial model has a lot of uncertainties, which will easily cause the iterative inversion process to lose in local minimum values, in severe case, even can result in the failure of the FWI algorithm.

Figure 16(a) displays the reconstructed thickness map for the double defects in section IV-B by the classical FWI method. It is worth noting that only the high-frequency exciting data (center frequency is 70 kHz) measured in section IV-B is used. Compared the inverted thickness map in Figure 16(a) with the original thickness model in Figure 14(a), we can find that the shape and outline of the defects have obvious differences. This may be influenced by the absence of low-frequency data (center frequency is 50 kHz). Figure 16(b) shows the inverted thickness map for the double defects by the auto-calibration method. The same as Figure 16(a), only the high-frequency data is used. However, with the help of the macro initial model by the ray tomography, the imaging results shows fairly accuracy with the inverted result in Figure 14(d) (both low- and high-frequency exciting data are used). The cross-section thickness distributions in Figure 16(c) and 16(d) state that the imaging accuracy using only high-frequency data is higher than that using only low-frequency data, but slightly lower than that using the full band data. This is acceptable because broadband data facilitates imaging results. The global relative errors of the imaging results are shown in Table 3, which also demonstrates that the auto-calibration algorithm enhances the robustness of the FWI algorithm and improves the imaging accuracy when data bandwidth is limited.

V. CONCLUSION

This study proposes a hybrid GWT method by a combination of the ray tomography and FWI method. Both synthetic and experimental imaging results show that the new method can obtain a smaller global error (difference between the original and inverted thickness map) than the classical method, which further illustrates the applicability and practicability of the new method. The two main improvement of the new method is as follows:

(1) Compared with the classical method (artificial selection method), the risk of the wrong selection greatly decreases and, with the help of ray tomography reconstruction result, the new method enables the automatic selection of the reference signal to calibrate the forward modeling error caused by using the acoustic equation approximation in the FWI process.

(2) The good imaging results of the complex and irregular defects at the absence of the low-frequency data valid that, using the macro model inverted by the ray tomography method as the initial model of the FWI algorithm can significantly decrease the possibility of losing in local minimum values and enhance the robustness of the FWI method.

REFERENCES

[1] X. Li, D. Zhang, Z. Liu, Z. Li, C. Du, and C. Dong, "Materials science: Share corrosion data," *Nature*, vol. 527, no. 7579, pp. 441–442, Nov. 2015.

[2] W. Xu, B. Zhang, Y. Deng, Z. Wang, Q. Jiang, L. Yang, and J. Zhang, "Corrosion of rail tracks and their protection," *Corrosion Rev.*, vol. 39, no. 1, pp. 1–13, Feb. 2021.

[3] D. Sueseenak, T. Chanwimalueang, W. Narkbuekaew, K. Chitsakul, and C. Pintavirooj, "Cone-beam X-ray tomography with arbitrary-orientation X-ray tube," in *Proc. 1ST IEEE Conf. Ind. Electron. Appl.*, May 2006, pp. 1–4.

[4] Y. Ma, Q. Wang, L. Pei, and J. Zhang, "Application of acoustic emission technique on strength test of composite fuselage ring," in *Proc. 16th Symp. Piezoelectricity, Acoustic Waves, Device Appl. (SPAWDA)*, Oct. 2022, pp. 784–787.

[5] I. T. Gürbüz, P. Rasilo, F. Martin, O. Osemwinyen, and A. Belahcen, "2-D analytical model for computing eddy-current loss in nonlinear thick steel laminations," *IEEE Trans. Magn.*, vol. 58, no. 9, pp. 1–4, Sep. 2022.

[6] M. K. ElBatanouny, J. Mangual, W. Vélez, P. H. Ziehl, F. Matta, and M. González, "Monitoring corrosion in prestressed concrete beams using acoustic emission technique," in *Proc. SPIE*, vol. 8347, 2012, pp. 278–287.

[7] F. Honarvar and A. Varvani-Farahani, "A review of ultrasonic testing applications in additive manufacturing: Defect evaluation, material characterization, and process control," *Ultrasonics*, vol. 108, Dec. 2020, Art. no. 106227.

[8] C. Pei, T. Fukuchi, H. Zhu, K. Koyama, K. Demachi, and M. Uesaka, "A study of internal defect testing with the laser-EMAT ultrasonic method," *IEEE Trans. Ultrason., Ferroelectr., Freq. Control*, vol. 59, no. 12, pp. 2702–2708, Dec. 2012.

[9] X. Zhao, R. L. Royer, S. E. Owens, and J. L. Rose, "Ultrasonic Lamb wave tomography in structural health monitoring," *Smart Mater. Struct.*, vol. 20, no. 10, Aug. 2011, Art. no. 105002.

[10] W. Xu, M. Yuan, W. Xuan, X. Ji, and Y. Chen, "Quantitative inspection of complex-shaped parts based on ice-coupled ultrasonic full waveform inversion technology," *Appl. Sci.*, vol. 11, no. 10, p. 4433, May 2021.

[11] J. C. P. McKeon and M. K. Hinders, "Parallel projection and crosshole Lamb wave contact scanning tomography," *J. Acoust. Soc. Amer.*, vol. 106, no. 5, pp. 2568–2577, Nov. 1999.

[12] E. V. Malyarenko and M. K. Hinders, "Fan beam and double crosshole Lamb wave tomography for mapping flaws in aging aircraft structures," *J. Acoust. Soc. Amer.*, vol. 108, no. 4, pp. 1631–1639, Oct. 2000.

[13] P. Belanger, P. Cawley, and F. Simonetti, "Guided wave diffraction tomography within the born approximation," *IEEE Trans. Ultrason., Ferroelectr., Freq. Control*, vol. 57, no. 6, pp. 1405–1418, Jun. 2010.

[14] P. Huthwaite, "Evaluation of inversion approaches for guided wave thickness mapping," *Proc. Roy. Soc. A, Math., Phys. Eng. Sci.*, vol. 470, no. 2166, Jun. 2014, Art. no. 20140063.

[15] P. Huthwaite and F. Simonetti, "High-resolution guided wave tomography," *Wave Motion*, vol. 50, no. 5, pp. 979–993, Jan. 2021.

[16] P. Huthwaite, A. A. Zwiebel, and F. Simonetti, "A new regularization technique for limited-view sound-speed imaging," *IEEE Trans. Ultrason., Ferroelectr., Freq. Control*, vol. 60, no. 3, pp. 603–613, Mar. 2013.

[17] J. Virieux and S. Operto, "An overview of full-waveform inversion in exploration geophysics," *Geophysics*, vol. 74, no. 6, pp. WCC1–WCC26, Nov. 2009.

[18] R. G. Pratt and M. H. Worthington, "Inverse theory applied to multi-source cross-hole tomography. Part 1: Aoustic wave-equation method," *Geophys. Prospecting*, vol. 38, no. 3, pp. 287–310, Apr. 1990.

[19] S. Bernard, V. Monteiller, D. Komatitsch, and P. Lasaygues, "Ultrasonic computed tomography based on full-waveform inversion for bone quantitative imaging," *Phys. Med. Biol.*, vol. 62, no. 17, pp. 7011–7035, Aug. 2017.

[20] M. Pérez-Liva, J. L. Herraiz, J. M. Udías, E. Miller, B. T. Cox, and B. E. Treeby, "Time domain reconstruction of sound speed and attenuation in ultrasound computed tomography using full wave inversiona)," *J. Acoust. Soc. Amer.*, vol. 141, no. 3, pp. 1595–1604, Mar. 2017.

[21] J. Rao, M. Ratassepp, and Z. Fan, "Guided wave tomography based on full waveform inversion," *IEEE Trans. Ultrason., Ferroelectr., Freq. Control*, vol. 63, no. 5, pp. 737–745, May 2016.

[22] J. Rao, M. Ratassepp, and Z. Fan, "Limited-view ultrasonic guided wave tomography using an adaptive regularization method," *J. Appl. Phys.*, vol. 120, no. 19, Nov. 2016, Art. no. 194902.

[23] J. Rao, J. Yang, M. Ratassepp, and Z. Fan, "Multi-parameter reconstruction of velocity and density using ultrasonic tomography based on full waveform inversion," *Ultrasonics*, vol. 101, Feb. 2020, Art. no. 106004.

[24] T. D. Nguyen, K. T. Tran, and N. Gucunski, "Detection of bridge-deck delamination using full ultrasonic waveform tomography," *J. Infrastruct. Syst.*, vol. 23, no. 2, Jun. 2017, Art. no. 04016027.

[25] J. He, J. Rao, J. D. Fleming, H. N. Gharti, L. T. Nguyen, and G. Morrison, "Numerical ultrasonic full waveform inversion (FWI) for complex structures in coupled 2D solid/fluid media," *Smart Mater. Struct.*, vol. 30, no. 8, Aug. 2021, Art. no. 085044.

[26] L. T. Nguyen and R. T. Modrak, "Ultrasonic wavefield inversion and migration in complex heterogeneous structures: 2D numerical imaging and nondestructive testing experiments," *Ultrasonics*, vol. 82, pp. 357–370, Jan. 2018.

[27] M. Ratassepp, J. Rao, X. Yu, and Z. Fan, "Modeling the effect of anisotropy in ultrasonic-guided wave tomography," *IEEE Trans. Ultrason., Ferroelectr., Freq. Control*, vol. 69, no. 1, pp. 330–339, Jan. 2022.

[28] T. Druet, J.-L. Tastet, B. Chapuis, and E. Moulin, "Autocalibration method for guided wave tomography with undersampled data," *Wave Motion*, vol. 89, pp. 265–283, Jun. 2019.

[29] W. S. Zhang, J. Luo, and J. W. Teng, "Frequency multiscale full-waveform velocity inversion," *Chin. J. Geophys.*, vol. 58, no. 1, pp. 216–228, Jan. 2015.

[30] C. Jo, C. Shin, and J. H. Suh, "An optimal 9-point, finite-difference, frequency-space, 2-D scalar wave extrapolator," *Geophysics*, vol. 61, no. 2, pp. 529–537, Mar. 1996.

[31] A. Guitton and W. W. Symes, "Robust inversion of seismic data using the Huber norm," *Geophysics*, vol. 68, no. 4, pp. 1310–1319, Jul. 2003.

[32] J. Rao, M. Ratassepp, and Z. Fan, "Investigation of the reconstruction accuracy of guided wave tomography using full waveform inversion," *J. Sound Vibrat.*, vol. 400, pp. 317–328, Jul. 2017.
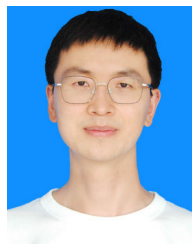
CAN JIANG received the B.S. degree from Jilin University, Changchun, China, in 2014, and the Ph.D. degree from the China University of Petroleum, Qingdao, China, in 2020. He is currently a Postdoctoral Fellow with the Institute of Acoustics, Chinese Academy of Sciences, Beijing, China. His main research interests include ultrasonic guided wave propagation mechanism and imaging.

YUBING LI received the B.S. degree in geophysics from Tongji University, Shanghai, China, in 2011, the master's degree in geophysics from Paris Diderot University, Paris, France, in 2014, and the Ph.D. degree in geoscience and geo-engineering from PSL Research University, Paris, in 2018. He is currently an Associate Professor with the Institute of Acoustics, Chinese Academy of Sciences, Beijing, China. His research interests include acoustic imaging, signal processing, and inverse problem.

HAO CHEN received the B.S. degree from Northeast Petroleum University, Daqing, China, in 1991, the M.S. degree from the North China University of Technology, Beijing, China, in 2004, and the Ph.D. degree from the Institute of Acoustics, Chinese Academy of Sciences, Beijing, in 2007. He is currently a Master's Tutor with the Institute of Acoustics, Chinese Academy of Sciences. His main research interests include acoustic logging and acoustic signal processing.

WEIWEI MA received the B.S. degree from the Minzu University of China, Beijing, China, in 2013, and the master's degree from the University of Chinese Academy of Sciences, Beijing, in 2016. She is currently an Engineer with the Institute of Acoustics, Chinese Academy of Sciences, Beijing. Her main research interest includes acoustic logging instrumentation development.

JIAWEI WEN received the B.S. degree from Nanchang Hangkong University, Nanchang, China, in 2019. He is currently pursuing the Ph.D. degree with the Institute of Acoustics, Chinese Academy of Sciences, Beijing, China. His main research interest includes ultrasonic guided wave imaging.

JIAN WANG (Member, IEEE) received the B.S. degree in geophysics from the China University of Geosciences, Beijing, China, in 2014, and the Ph.D. degree, in 2018. He did postdoctoral research work with the Institute of Geology and Geophysics, Chinese Academy of Sciences, Beijing. He is currently an Associate Researcher with the Institute of Acoustics, Chinese Academy of Sciences. His main research interest includes acoustic imaging.

• • •